ISSN 8755-6839

SCIENCE OF TSUNAMI HAZARDS

Journal of Tsunami Society International

Volume 41 Number 4 2022

RUPTURE KINEMATIC PROCESS OF THE MW 5.9 SERAM EARTHQUAKE IMAGED BY BACK-PROJECTION TECHNIQUE FOLLOWED BY THE TSUNAMI

Muhammad Nurul Fahmi*, Arie Realita, and Madlazim

Physics Department, Faculty of Mathematics and Natural Sciences, Universitas Negeri Surabaya, Surabaya 60231, Indonesia

*muhammadfahmi@unesa.ac.id

ABSTRACT

The 16 June 2021 Seram earthquake occurred at a moderate magnitude of Mw 5.9 along the Banda Arc close to Seram Island, followed by a tsunami with a runup height of 0.51 m. A detailed kinematic study of the earthquake helps us better understand the tectonic environment of the secondary faults and the causes of an unexpected tsunamis after earthquakes, particularly on the island. In this study, we image the rupture processes of this earthquake using a Multiple Signal Classification Back-Projection (MUSIC-BP) method. This method used P-seismic waveforms from teleseismic data recorded by seismic stations across the Australian continent (AU arrays). These waveforms were filtered in the range of 0.5-1.0 Hz to remove unwanted phases. Our results show that the rupture moves bilaterally to southwest and northeast at a relatively slow speed of 1.47 km/s. In this earthquake, the rupture propagated ~35 km away from the epicenter and had a total duration of ~30 s. The maximum peak of the energy released is estimated to be ~15 km from the epicenter. The rupture directivity agrees well with the spatial distribution of aftershock events and the reported focal mechanism solution. According to the result of the rupture kinematics parameter, the tsunami was not caused directly by the earthquake. However, the direction of tsunami propagation is the same as that of earthquake rupture propagation. Furthermore, the results of this study reveal that the seismogenic fault under Seram Island has an SSW-NNE fault orientation.

Keywords: *Seram earthquake, Rupture processes, MUSIC-BP, AU arrays, tsunami*

1. INTRODUCTION

Eastern Indonesia is a region with a high level of seismicity because this region has complex tectonic environments caused by the interaction of the Pacific, Sunda, and Australian plates. The Banda Arc is where earthquakes occur most frequently, consisting of an inner volcanic arc, outer arc island, and trough (Hamilton, 1979; Spakman and Hall, 2010). In the outer Banda arc, there are several islands where earthquakes frequently occur: Seram, Haruku, Saparua, and Ambon islands. All islands adjacent to the Seram Trench's northern part always experience moderate to large earthquakes (Irsyam etal., 2020). Most recently, an earthquake occurred on 16 June 2019, located at the top of the Banda Arc on Seram Island, which resulted in a tsunami, and it is still unclear what caused it.

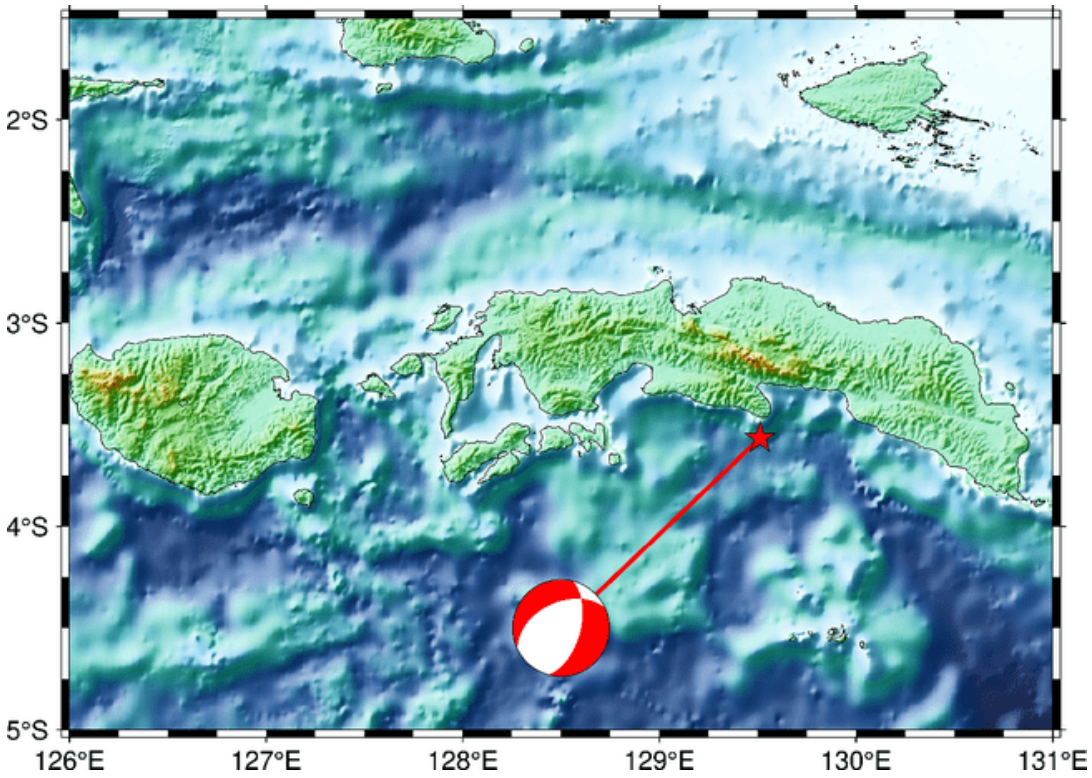

***Figure 1**. Location of the 16 June 2021 M_w 5.9 Seram Earthquake.*

On 16 June 2021 at 04:43:07 UTC, a moderate shallow earthquake occurred near Seram Island, triggering an unexpected tsunami(Figure 1). This was confirmed by the National Center for Environment Information (NOAA) (https://www.ngdc.noaa.gov/hazard/tsu_db.shtml) which reported that this earthquake caused a small tsunami with a runup height of 0.5 m. In general, moderate earthquakes infrequently generate large tsunami waves. Even if it could generate a tsunami, the runup would be unnoticeable and the amplitude would be only a few centimeters. Mainly this earthquake is located at the top of Banda Arc and the epicenter of this earthquake at 3.56^o S, 129.51^o E, with a depth of 9.95 km. The moment tensor of Global-Centroid-Moment-Tensor (Global CMT, 2022; Ekström et al., 2012) provides a focal mechanism indicating a normal fault mechanism, where the nodal plane 1 (NP1) with strike1 = 245^o, dip1 = 46^o,

rake1 = -50^{o}; and nodal plane 2 (NP2) with strike1 = 14^{o}, dip1 = 57^{o}, rake1 = -124^{o}. In addition, Global CMT positioned the centroid of the mainshock at a depth of 14.3 km. This moderate earthquake occurs in an area with complex geological conditions and can cause unexpectedly large tsunamis. Thus, rupture imaging is a solution to determine the kinematics of earthquake rupture and causes of unexpected tsunamis.

The kinematics rupture process of the earthquake can be known based on recording high-frequency (HF) seismic waveforms from the analysis using the Back-Projection (BP) method. This method uses an array signal processing technique to analyze the seismic waves recorded on dense seismic networks (Ishii et al., 2005; Krüger and Ohrnberger. 2015; Ishii et al., 2007). Thus, it can image the position of the rupture propagation and obtain a spatiotemporal distribution image of the earthquake source. The BP method produces robust resolution at each time frame since it only utilizes array processing and ignores fault geometry or Greens function assumptions. The BP method has been successfully applied to recent studies of large earthquakes worldwide (Kiser et al., 2011; Meng et al., 2011; Meng et al., 2012; Yao et al., 2012; Fan and Shearer, 2015; Liu et al., 2017; Wong et al., 2018; Bao et al., 2019; Xie and Meng, 2020; Kehoe and Kiser. 2020; Kiser and Kehoe, 2021; Madlazim et al., 2021; Sultan et al., 2022). Thus, this method is excellent and accurate for revealing earthquake rupture kinematics.

One of the accurate and high-resolution back-projection methods is the Multiple Signal Classification Back-Projection (MUSIC-BP) method developed by (Meng et al., 2011, Meng et al., 2016). The first thing to use the MUSIC-BP method is to evaluate the covariance matrix of the waveform in each sliding time window and sampling frequency. The steering vector which consists of travel time shift at each station is calculated for each candidate source node. The direction of arrival corresponding to the most probable source location is then determined by the maximum amplitude of the MUSIC pseudospectrum, which is defined as the inversion of the steering vector projection to the subspace noise (Schmidt, 1986). In a previous study, Bao et al. (2019) revealed the direction of rupture propagation and persistent supershear rupture speed from the 2018 Palu earthquake using the MUSIC-BP method. In addition, Madlazim et al. (2021) used the same method to determine the direction of propagation and low-velocity rupture that caused the tsunami in the Aegean Sea.

In this study, we adopted the multitaper back-projection (MUSIC BP) method (Meng et al., 2011, Meng et al., 2016) to investigate the rupture kinematics for the Seram earthquake. The position of the seismic source of an earthquake is determined by time shifts and a collection of waveforms (stacked waveforms) recorded at the teleseismic distance to the grid from the potential source location as a function of time (Ishii et al., 2005; Krüger and Ohrnberger, 2005). Based on this information, parameters of rupture kinematics (rupture direction, speed, and length) dan direction of tsunami propagation can be estimated. We also compared our result with a relevant previous study.

2. METHOD

The back-projection method can be utilized with any seismic station network and any seismic phase, while P waves recorded at teleseismic distances are most commonly

used for most earthquakes due to little interference with other seismic phases. The method is most commonly applied to seismic arrays with dense station spacing and a small overall aperture. Because the wave pathways from the source to the receivers are comparable in these circumstances, the recorded waveforms are coherent across the array. The waveform coherence improves the stacking process and quickly removes artefacts from the source image. While using a single array yields reliable results, the small aperture limits spatial and temporal resolution. Increased distribution of seismic stations can result in better resolution, although care must be given to minimize source image artefacts caused by incoherent data. Visual assessment of the data or a measure of similarity between waveform segments is frequently used (for example, correlation values). While picking data based on waveform features can be beneficial, this method ignores the sources of artefacts in back-projection results.

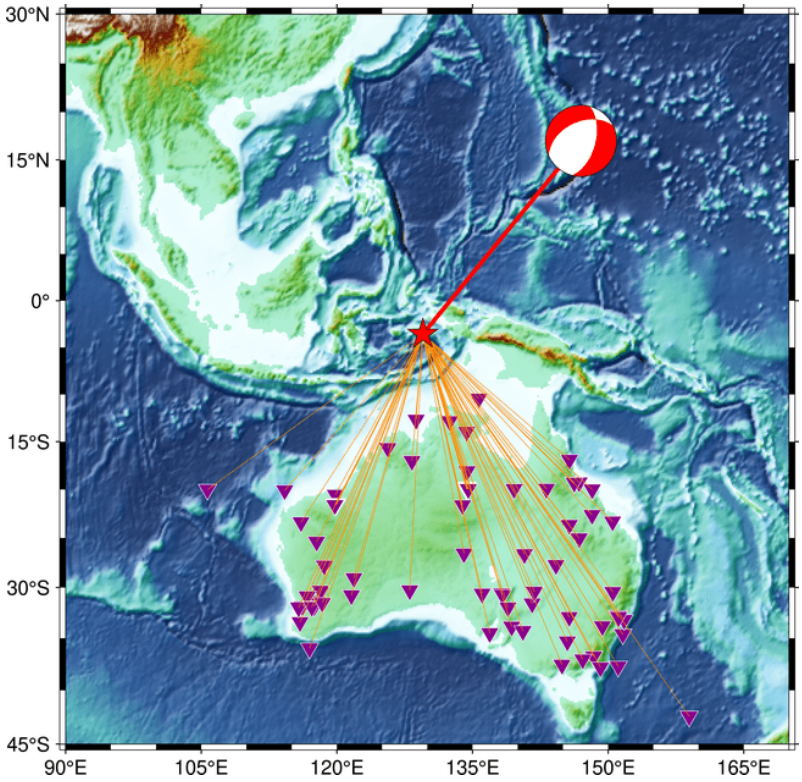

Figure 2. *AU array location that recorded P-seismic waveforms from Seram earthquake.*

In this study, Multiple Signal Classification Back-Projection (Meng et al., 2011; Bao et al., 2019), an array processing approach, was used. P-seismic waveform from a wide distribution of Australian teleseismic stations (AU array) was used to describe the rupture properties of the Seram earthquake on 16 June 2021 (Figure 2). The epicenter distance from the AU array is about 50^{o} for better rupture imaging results. The initial step for rupture process imaging using MUSIC-BP is 60 seconds first time window from the arrival of the P-seismic waveform as this method's input process. Nevertheless, the amplitude of the P-seismic waveform is affected by the radiation pattern (noise). Back projection rupture imaging with MUSIC prioritizes tracking the most coherent phases within the time window. Furthermore, alignment is performed on the first arrivals of the P-seismic

waveform so that the lateral velocity variations for each waveform become coherent (Goldstein and Archuleta 1987). After the alignment, the high-frequency P-seismic waveforms are filtered at a range of 0.5 to 1 Hz, as this is the highest band where coherent arrival initials must be closely aligned. This step applies an empirical travel time correction to the data, ensuring that the P-seismic waveforms arrive at the same time as predicted by the one-dimensional Earth model (IASP91) (Kennett and Engdahl, 1991). This step additionally corrects waveform polarities and normalizes P-seismic waveform amplitudes such that the initial waveforms have the same polarity. This technique is better than previous methods, such as the beamforming technique (Rost and Thomas, 2002) and this method not only produces a rupture imaging model for large earthquakes but can also be used for moderate earthquakes (Jian, 2021; Meng et al., 2020).

3. RESULTS AND DISCUSSION

MUSIC-BP analysis was applied to the Seram earthquake to determine the kinematic rupture process, where the rupture kinematics consisted of the parameters of rupture, namely rupture directivity, rupture length, rupture duration, and rupture speed. The back-projection results are integrated with the AU arrays to reconstruct the imaging rupture results from this earthquake. The P-seismic waveforms recorded by the AU arrays are filtered in the frequency range of 0.5-1.0 Hz. The filter range selection is based on the fact that teleseismic waveforms accommodate much noise and then a higher frequency is needed to obtain acceptable seismic waveforms [29].

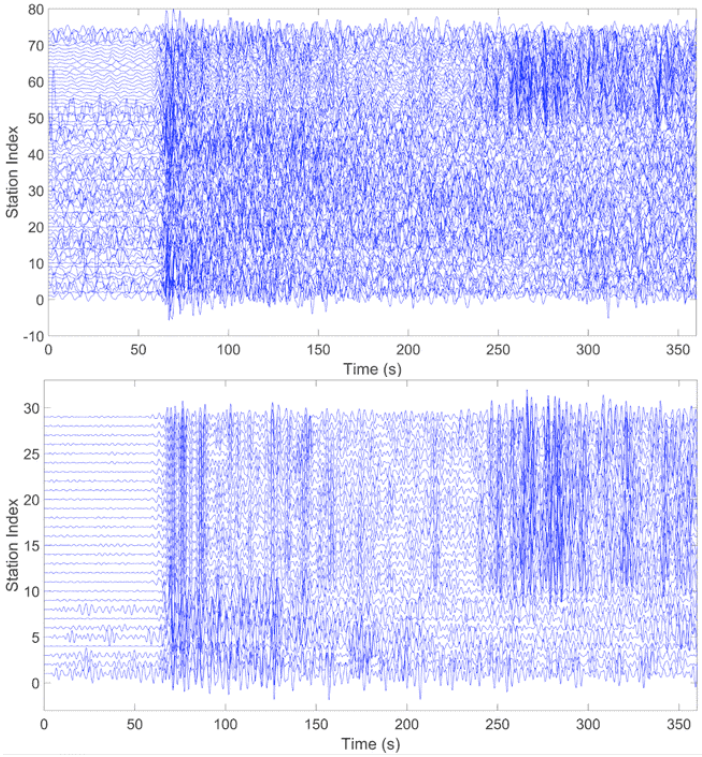

Figure 3. *Seismogram of AU array. a) unfiltered seismogram and b) filetered coherent seismogram.*

Figure 2a demonstrates an unfiltered seismogram (raw data) and Figure 2b describes a filtered coherent seismogram. The filtered coherent seismogram is used as the initial process for imaging rupture processes (Ishii et al., 2007; Meng et al., 2018; Zeng et al., 2019). The smoother and more coherent the filtered seismogram provides better results for rupture imaging. It can be seen that the filtered seismogram of each station in the AU array has the same initial phase and lower noise (compared to unfiltered seismograms), which can reduce the uncertainty of rupture imaging results. Thus, the initial step of MUSIC-BP processing obtained good results and can be used to determine the kinematic rupture process of the Seram earthquake.

The rupture imaging results from the filtered coherent seismogram processed using the MUSIC-BP method can be seen in Figure 4. Processing using the AU array on the Seram earthquake can produce better imaging because almost all stations on the Australian continent work well. AU array distance is relatively closer than other arrays, so it has acceptable seismograms, so the seismogram data set is used as acceptable input for MUSIC-BP.

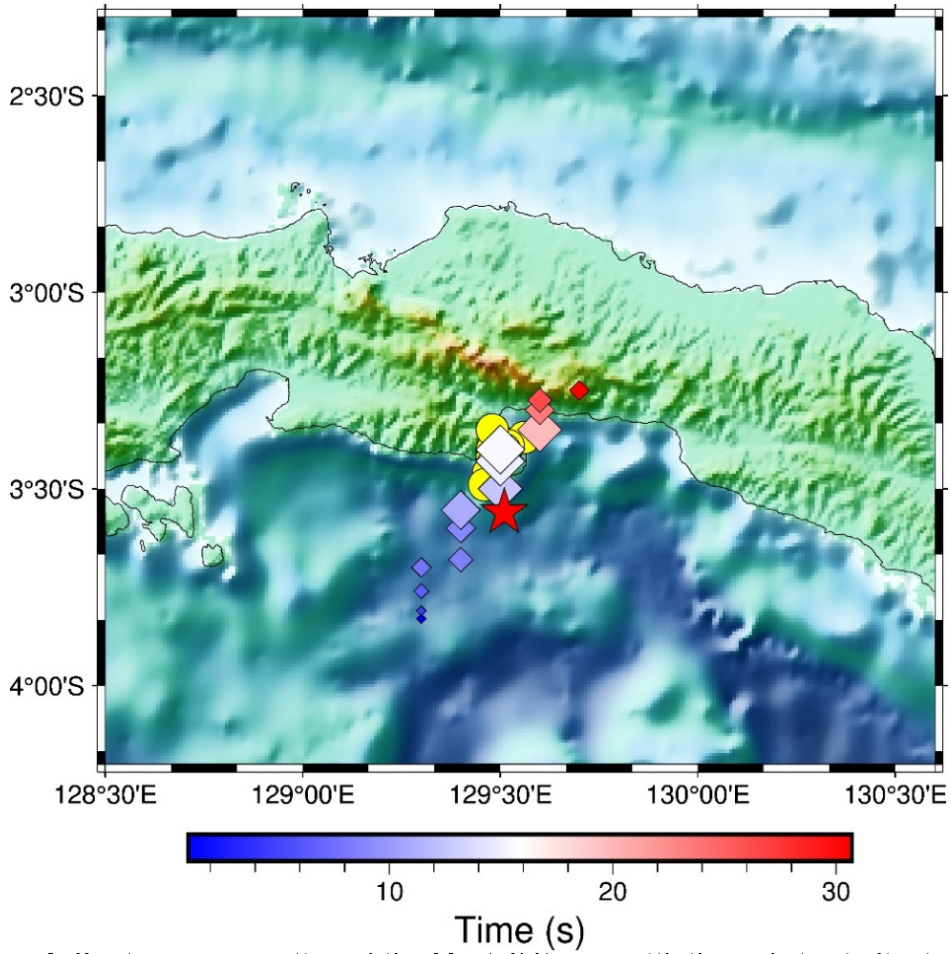

***Figure 4**. Rupture propagation of the Mw 5.9 Seram with the red star indicates the epicenter, the orange circle is the distribution of aftershocks and the gradation coloured diamond demonstrated rupture propagation.*

It is clear that the rupture imaging results for this earthquake (Figure 4) have a bilateral distribution of shear rupture, where the direction of rupture propagation is towards the southwest and northeast (gradation colored diamond). This is confirmed by the presence of aftershocks (orange circle) along the rupture trajectory. The majority of aftershock has a magnitude between 4 and 5 with shallow depth. The well-located aftershocks are associated with the direction of rupture propagation (Yukutake and Iio, 2017) because the presence of aftershocks is caused by changes in coseismic stress in the fault segmentation around the earthquake epicenter [33, 34]. In addition, the direction of rupture propagation can be used to determine active faults in the study area. If the rupture directivity in this study is correlated with the results of the Global CMT focal mechanism solution, then the actual fault plane is indicated to have a strike angle of 245^{o}. Thus, the activated fault plane of the Mw 5.9 Seram earthquake is NP 1 with a fault plane orientation consisting of strike1 = 245^{o}, dip1 = 46^{o}, and rake1 = -50^{o} with a normal fault type. Note that the orientation parameter of the fault plane at NP 1 shows that the dip parameter has a low angle value. Based on previous research conducted by (Cummins et al., 2020) stated that the characteristics of earthquakes that occur in the Banda Sea area (covering the bottom of Seram Island) have a low dip angle value termed as the Low-Angle Normal Fault (LANF) which can cause a tsunami due to earthquake-triggered slumping. This finding reveals that there is an activated fault in the area under the island of Seram, which often causes earthquakes with shallow depths. This also indicates that this island has a shallow tectonic structure with potential earthquake and tsunami hazards.

Rupture directivity is the result of the rupturing movement of the earthquake source. Rupture movement has a certain speed that is correlated with the energy released from the earthquake source, where the rupture speed and earthquake energy are positively correlated (Noda et al., 2011; Weng and Ampuero, 2020). The previous paragraph only describes the orientation of the rupture propagation of the earthquake but does not explain the rupture's length, duration, speed and energy when it propagates. Here, we plot the relationship between rupture length (spatial parameter) and rupture propagation duration (temporal parameter) with respect to the relative amplitude (Figure 5).

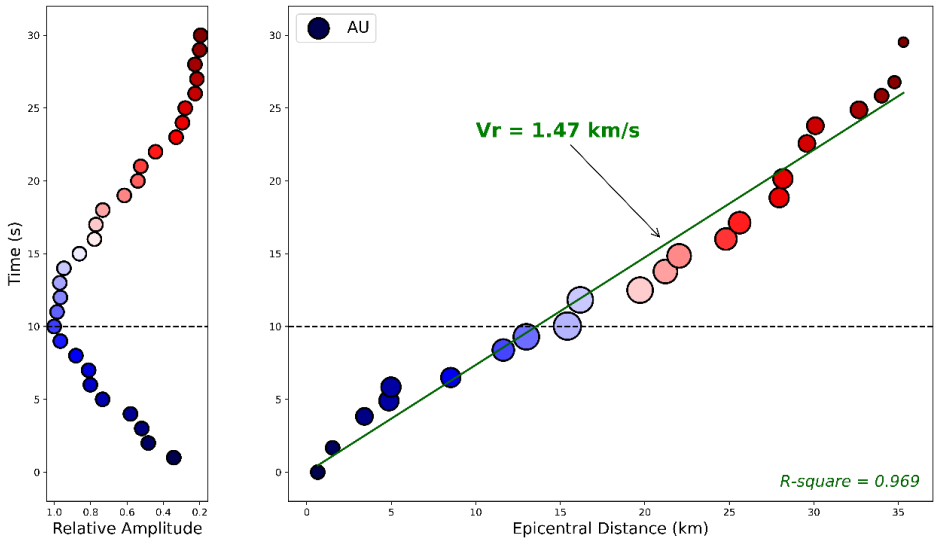

***Figure 5**. The spatio-temporal variations of rupture kinematic*

The top panel describes the time-varying normalised amplitude of the bilaterally moving rupture in the southwest and northeast directions. During this time, the peak of seismic energy is released from the earthquake source in the first 15 seconds (black dashed line). This correlates with the visualisation with the bottom panel which describes the largest circle size depicted at 15 seconds with rupture propagating for about 15 km in the northeast direction (See Figure 4). Thus, it can be mentioned that the northeast area of the earthquake epicenter has a higher energy release rate because of the high stress changes and local fault activity (Hutchings and Mooney, 2021). The total rupture length is approximately 70 km from the southwest to the northeast (35 km from the epicenter) with a total duration of about 18 s. A moderate earthquake has lower energy than a large earthquake, so the rupture extent is not too long and has a relatively short duration. Furthermore, the rupture velocity of this earthquake is 1.5 km/s which is obtained from spatiotemporal variations of rupture kinematics through a linear regression approach (Meng et al., 2011; Bao et al., 2019). This result are consistent with previous studies which stated that the rupture velocity for moderate earthquakes was 0.5-0.9 of the shear wave (Seekins and Boatwright, 2010).

The lower region of the Seram earthquake has a complex tectonic setting and there are active minor faults in the region that have not been identified. The kinematic rupture processes in this study indicate that the source mechanism of the earthquake has an SSW-NNE orientation direction and has a low dip angle of the focal mechanism. Based on Cummins et al. (2020) stated that if an earthquake has a low dip angle value, then the earthquake can trigger a tsunami. However, according to Heidarzadeh et al. (2022), using numerical tsunami modeling, the tsunami in this event was not directly caused by this earthquake but by a submarine landslide. Referring to the rupture parameters in this study, the rupture duration and rupture length indicate that this earthquake has no potential to cause a tsunami (Lomax and Michelini, 2011). Even though this earthquake did not directly generate a tsunami, the direction of the tsunami propagation towards the SSW-NNE was in the same direction as the orientation of the earthquake fault. Thus, it can be assumed that the earthquake that occurred could cause a landslide in the sea, so this submarine landslide was the primary source of the tsunami. This finding implies that if an earthquake occurs with a large magnitude, it is possible to cause a massive submarine landslide and also a devastating tsunami in the bottom area of Seram Island. Further work needs to be carried out to understand better the modeling of tsunami mechanisms and the direction of tsunami propagation in the region.

4. CONCLUSIONS

The 2021 Mw 5.9 Seram earthquake occurred along the Banda Arc near Seram Island. We have used the Multiple Signal Classification Back-Projection (MUSIC-BP) method to image the kinematic rupture processes of this earthquake. A High-frequency P-seismic waveform is processed to obtain rupture directivity, rupture duration, rupture length, and rupture speed. The rupture imaging shows that the rupture moves bilaterally to the southwest and northeast with a speed of 2.4 km/s. The total rupture length is ~70 km from southwest to northeast (~35 km from epicenter) and has a total duration of

about 18 s. The maximum amplitude energy of this earthquake released is estimated to be ~15 km from the epicenter. The observed main path of the rupture propagation is consistent with the position of the aftershock location distribution data. Based on the result of the rupture kinematics parameter, the tsunami was not caused directly by the earthquake. However, the direction of tsunami propagation is the same as that of earthquake rupture propagation. Thus, it can be assumed that the earthquake could cause a landslide in the sea, so this submarine landslide was the primary source of the tsunami. Furthermore, this study has revealed that the tectonic setting at the bottom of Seram Island has an SSW-NNE fault orientation

ACKNOWLEDGEMENTS

We thank Incorporated Research Institutions for Seismology (IRIS) for providing freely teleseismic earthquake seismogram data at https://ds.iris.edu/wilber3/find_event and the United States Geological Survey (USGS) for providing distribution aftershocks data accessed at https://earthquake.usgs.gov/earthquakes/search. We also thank Global Centroid-Moment-Tensor (GCMT) for information on earthquake focal mechanism data.

REFERENCES

Bao, H. et al. (2019). Early and persistent super shear rupture of the 2018 magnitude 7.5 Palu earthquake. *Nat. Geosci.*, vol. 12, pp. 200–205. https://doi.org/10.1038/s41561-018-0297-z

Cummins, P. R., Pranantyo, I. R., Pownall, J. M., Griffin, J. D., Meilano, I., & Zhao, S. (2020). Earthquakes and tsunamis caused by low-angle normal faulting in the Banda Sea, Indonesia. *Nat. Geosci.*, vol. 13, pp. 312–318. https://doi.org/10.1038/s41561-020-0545-x

Douglas, A. (1997). Bandpass filtering to reduce noise on seismograms: Is there a better way?. *Bull. Seismol. Soc. Am.*, vol. 87, no. 3, pp. 770–777. https://doi.org/10.1785/BSSA0870030770

Ekström, G., Nettles, M., & Dziewoński, A. M. (2012). The global CMT project 2004–2010: centroid-moment tensors for 13,017 earthquakes. *Phys. Earth Planet. Inter.*, vol. 200, pp. 1–9. https://doi.org/10.1016/j.pepi.2012.04.002

Fan, W & Shearer, P. M. (2015). Detailed rupture imaging of the 25 April 2015 Nepal earthquake using teleseismic *P* waves. *Geophys. Res. Lett.*, vol. 42, no. 144, pp. 5744–5752. https://doi.org/10.1002/2015GL064587

Global CMT, https://www.globalcmt.org/, acessed online on 2022.

Goldstein, P. & Archuleta, R. J. (1987). Array analysis of seismic signals. *Geophys. Res. Lett.*, vol. 14, no. 1, pp. 13–16. https://doi.org/10.1029/GL014i001p00013

Hamilton, W. B. (1979). *Tectonic of Indonesia Region, Geological Survey Professional Paper,* United States Government Printing Office. https://doi.org/10.3133/pp1078

Heidarzadeh, M., Gusman, A. R., Patria, A., & Widyantoro, B. T. (2022). Potential Landslide Origin of the Seram Island Tsunami in Eastern Indonesia on 16 June 2021 Following an Mw 5.9 Earthquake. *Bull. Seismol. Soc. Am.*, vol. 112 no. 5, pp. 2487–2498. https://doi.org/10.1785/0120210274

Hutchings, S. J. & Mooney, W. D. (2021). The Seismicity of Indonesia and Tectonic Implications. *Geochemistry, Geophys. Geosystems*, vol. 22, no. 9. https://doi.org/10.1029/2021GC009812

Irsyam, M. et al. (2020). Development of the 2017 national seismic hazard maps of Indonesia. *Earthq. Spectra*, vol. 36, no. S1, pp. 112–136. https://doi.org/10.1177%2F8755293020951206

Ishii, M., Shearer, P. M., Houston, H., & Vidale, J. E. (2005). Extent, duration and speed of the 2004 Sumatra‐Andaman earthquake imaged by the Hi‐Net array. *Nature*, vol. 435, pp. 933–936. https://doi.org/10.1038/nature03675

Ishii, M., Shearer, P. M., Houston, H., & Vidale, J. E. (2007). Teleseismic P wave imaging of the 26 December 2004 Sumatra–Andaman and 28 March 2005 Sumatra earthquake ruptures using the Hi-net array. *J. Geophys. Res., Solid Earth*, vol. 112, no. B11307. https://doi.org/10.1029/2006JB004700

Jian, P. R. (2021). The 2010 Jiashian and 2016 Meinong Earthquakes: Doublet Ruptures Interact Across Two Strong Asperities. In: AutoBATS and 3D MUSIC: New Approaches to Imaging Earthquake Rupture Behaviors. *Springer Theses*, Springer, Singapore. https://doi.org/10.1007/978-981-16-5584-5_5

Kehoe, H. L. & Kiser, E. D. (2020). Evidence of a supershear transition across a fault stepover. *Geophys. Res. Lett.*, vol. 47, no. 10. https://doi.org/10.1029/2020GL087400

Kennett, B. L. N. & Engdahl, E. R. (1991). Traveltimes for global earthquake location and phase identification. *Geophys J Int.*, vol. 105, no. 2, pp. 429–465. https://doi.org/10.1111/j.1365-246X.1991.tb06724.x

Kiser, E. D. & Kehoe, H. L. (2021). The hazard of coseismic gaps: the 2021 Fukushima earthquake," *Geophys J Int.*, vol. 227, no. 1, pp. 54–57. https://doi.org/10.1093/gji/ggab208

Kiser, E., Ishii, M., Langmuir, C. H., Shearer, P. M., & Hirose, H. (2011). Insights into the mechanism of intermediate-depth earthquakes from source properties as imaged by back projection of multiple seismic phases. *J. geophys. Res.*, vol. 116, no. B06310. https://doi.org/10.1029/2010JB007831

Krüger., F. & Ohrnberger, M. (2005). Tracking the rupture of the Mw = 9.3 Sumatra earthquake over 1,150 km at teleseismic distance. *Nature*, vol. 435, pp. 937–939. https://doi.org/10.1038/nature03696

Liu, Z., Song, C., Meng, L., Ge, Z., Huang, Q., & Wu, Q. (2017). Utilizing a 3D global P-wave tomography model to improve backprojection imaging: a case study of the 2015 Nepal earthquake. *Bull. Seismol. Soc. Am.*, vol. 107, no. 5, pp. 2459–24667. https://doi.org/10.1785/0120170091

Lomax, A. & Michelini, A. (2011). Tsunami early warning using earthquake rupture duration and *P*-wave dominant period: the importance of length and depth of faulting. *Geophys. J. Int.*, vol. 185 no. 1, pp. 283–291. https://doi.org/10.1111/j.1365-246X.2010.04916.x

Madlazim, Fahmi, M. N., Realita, A., & Sari, D. P. (2021). Rupture Imaging For The 30 October Tsunamigenic Earthquake In The Eastern Aegean Sea. Science of Tsunami. *Sci. Tsu. Hazard.*, vol. 40, no. 4, pp. 228–237. http://www.tsunamisociety.org/STHVol40N4Y2021.pdf

Meng , L., Bao, H., Huang, H., Zhang, A., Bloore, A., & Liu, Z. (2018). Double pincer movement: Encircling rupture splitting during the 2015 Mw 8.3 Illapel earthquake. *Earth Planet Sci Lett.*, vol. 495, pp. 164–173. https://doi.org/10.1016/j.epsl.2018.04.057

Meng, H., McGuire, J. J., & Ben-Zion, Y. (2020). Semiautomated Estimates of Directivity and Related Source Properties of Small to Moderate Southern California Earthquakes Using Second Seismic Moments. *J. Geophys. Res., Solid Earth*, vol. 125, no. 4. https://doi.org/10.1029/2019JB018566

Meng, L., Ampuero, J-P., Sladen, A., & Rendon, H. (2012). High-resolution backprojection at regional distance: application to the Haiti M7.0 earthquake and comparisons with finite source studies. *J. Geophys. Res., Solid Earth*, vol. 117, no. B4. https://doi.org/10.1029/2011JB008702

Meng, L., Inbal, A., & Ampuero, J-P. (2011). A window into the complexity of the dynamic rupture of the 2011 *Mw* 9 Tohoku‐Oki earthquake. *Geophys. Res. Lett.*, vol. 38, no. 7. https://doi.org/10.1029/2011GL048118

Meng, L., Zhang, A., & Yagi, Y. (2016). Improving back-projection imaging with a novel physics-based aftershock calibration approach: a case study of the 2015 Gorkha earthquake. *Geophys. Res. Lett.*, vol. 43, no. 2, pp. 628–636. https://doi.org/10.1002/2015GL067034

Neo, J. C., Huang, Y., Yao, D., & Wei, S. (2021). Is the Aftershock Zone Area a Good Proxy for the Mainshock Rupture Area?. *Bull. Seismol. Soc. Am.*, vol. 111, no. 1, pp. 424–438. https://doi.org/10.1785/0120190200

Noda, H., Lapusta, N., & Kanamori, H. (2011). Relation between energy radiation ratio and rupture speed in numerically simulated earthquakes. *AGU Fall Meeting*. https://ui.adsabs.harvard.edu/abs/2011AGUFM.S54C..03N/abstract

Rost, S. & Thomas, C. (2002). Array seismology: Methods and applications,. *Rev. Geophys.*, vol. 40, no. 3. https://doi.org/10.1029/2000RG000100

Schmidt, R. (1986). Multiple emitter location and signal parameter estimation. *IEEE Trans. Antennas Propag.*, vol. 34, no. 3, pp. 276–280. http://dx.doi.org/10.1109/TAP.1986.1143830

Seekins, L. C. & Boatwright, J. (2010). Rupture directivity of moderate earthquakes in northern California. *Bull. Seismol. Soc. Am.*, vol. 100 no. 3, pp. 1107–1119. https://doi.org/10.1785/0120090161

Segou, M. & Parsons, T. A new technique to calculate earthquake stress transfer and to probe the physics of aftershocks. (2020). *Bull. Seismol. Soc. Am.*, vol. 110, no. 2, pp. 863–873. https://doi.org/10.1785/0120190033

Spakman, W. & Hall, R. (2010). Surface deformation and slab–mantle interaction during Banda arc subduction rollback. *Nature Geosci*., vol. 3, no. 8, pp. 562–566. https://doi.org/10.1038/ngeo917

Sultan, M. et al. (2022). Imaging of rupture process of 2005 Mw 7.6 Kashmir earthquake using back projection techniques. *Arab J Geosci.*, vol. 15, no. 871. https://doi.org/10.1007/s12517-022-10095-5

Wang, D., Chen, Y., Wang, Qi., & Mori, J. (2018). Complex rupture of the 13 November 2016 M w 7.8 Kaikoura, New Zealand earthquake: Comparison of high-frequency and low-frequency observations. *Tectonophysics*, vol. 733, pp. 100–107. https://doi.org/10.1016/j.tecto.2018.02.004

Weng, H., & Ampuero, J-P. (2020). Continuum of earthquake rupture speeds enabled by oblique slip. *Nat. Geosci.*, vol. 13, pp. 817–821. https://doi.org/10.1038/s41561-020-00654-4

Xie, Y & Meng, L. (2020). A multi-array back-projection approach for tsunami warning. *Geophys. Res. Lett.*, vol. 47, no. 14. https://doi.org/10.1029/2019GL085763

Yao, H., Shearer, P. M., & Gersoft, P. (2012). Subevent location and rupture imaging using iterative back projection for the 2011 Tohoku M_w 9.0 earthquake," *Geophys J Int.*, vol. 190, no. 2, pp. 1152–1168. https://doi.org/10.1111/j.1365-246X.2012.05541.x

Yukutake, Y. & Iio, Y. (2017). Why do aftershocks occur? Relationship between mainshock rupture and aftershock sequence based on highly resolved hypocenter and focal mechanism distributions. *Earth, Planets Space,* vol. 69, no. 68. https://doi.org/10.1186/s40623-017-0650-2

Zeng, H., Wei, S., & Wu, W. (2019). Sources of uncertainties and artefacts in back-projection results. *Geophys J Int.*, vol. 220, no. 2, pp. 876–1891. https://doi.org/10.1093/gji/ggz482